

# Radiation hydrodynamics simulations of wide-angle outflows from super-critical accretion disks around black holes

Katsuya HASHIZUME \*

*School of Physical Sciences, Graduate University of Advanced Study (SOKENDAI), Shonan Village, Hayama, Kanagawa 240-0193, Japan*

*katsuya.hashizume@nao.ac.jp*

Ken OHSUGA

*National Astronomical Observatory of Japan, Osawa, Mitaka, Tokyo 181-8588, Japan*

*School of Physical Sciences, Graduate University of Advanced Study (SOKENDAI), Shonan Village, Hayama, Kanagawa 240-0193, Japan*

*ken.ohsugab@nao.ac.jp*

Tomohisa KAWASHIMA

*Key Laboratory for Research in Galaxies and Cosmology, Shanghai Astronomical Observatory, Chinese Academy of Science, 80 Nandan Road, Shanghai 200030, China*

*National Astronomical Observatory of Japan, Osawa, Mitaka, Tokyo 181-8588, Japan*

*kawashima-t@shao.ac.cn*

and

Masaomi TANAKA

*National Astronomical Observatory of Japan, Osawa, Mitaka, Tokyo 181-8588, Japan*

*School of Physical Sciences, Graduate University of Advanced Study (SOKENDAI), Shonan Village, Hayama, Kanagawa 240-0193, Japan*

*masaomi.tanaka@nao.ac.jp*

(Received ; accepted )

## Abstract

By performing two-dimensional radiation hydrodynamics simulations with large computational domain of 5000 Schwarzschild radius, we revealed that wide-angle outflow is launched via the radiation force from the super-critical accretion flows around black holes. The angular size of the outflow, of which the radial velocity ( $v_r$ ) is over the escape velocity ( $v_{\text{esc}}$ ), increases with an increase of the distance from the black hole. As a result, the mass is blown away with speed of  $v_r > v_{\text{esc}}$  in all direction except for the very vicinity of the equatorial plane,  $\theta = 0^\circ - 85^\circ$ , where  $\theta$  is the polar angle. The mass ejected from the outer boundary per unit time by the outflow is larger than the mass accretion rate onto the black hole,  $\sim 150L_{\text{Edd}}/c^2$ , where  $L_{\text{Edd}}$  and  $c$  are the Eddington luminosity and the speed of light. Kinetic power of such wide-angle high-velocity outflow is comparable to the photon luminosity and is a few times larger than the Eddington luminosity. This corresponds to  $\sim 10^{39} - 10^{40}$  erg s $^{-1}$  for the stellar mass black holes. Our model consistent with the observations of shock excited bubbles observed in some ultra-luminous X-ray sources (ULXs), supporting a hypothesis that ULXs are powered by the super-critical accretion onto stellar mass black holes.

**Key words:** accretion, accretion disks—black hole physics—ISM: jets and outflows—X-rays: galaxies

## 1. Introduction

Astrophysical black holes, such as active galactic nuclei, black hole binaries, and possibly gamma-ray bursts, are thought to be powered by disk accretion flows (accretion disks). From a theoretical point of view, the disks are known to exhibit three distinct modes according to the mass accretion rate; standard disk (Shakura & Sunyaev 1973), radiatively inefficient accretion flow /advection dominated accretion flow (Ichimaru 1977; Narayan & Yi 1994), and slim disk (Abramowicz et al. 1988). The slim disk appears when the accretion rate is much larger

than the critical rate,  $L_{\text{Edd}}/c^2$ , where  $L_{\text{Edd}}$  and  $c$  are the Eddington luminosity and the speed of light. Sądowski (2009) has reported that the standard disk turns into the slim disk at the accretion rate of  $L_{\text{Edd}}/(c^2\eta_a)$ , where the efficiency,  $\eta_a$ , is around 0.1 or less and is a function of a spin parameter of the black hole. The slim disk can shine above the Eddington luminosity in contrast to that the disk luminosities of standard disk and radiatively inefficient accretion flow are less than the Eddington luminosity. The slim disk basically succeeded in reproducing the observed features of ultra-luminous X-ray sources (ULXs) and narrow-line Seyfert 1 galaxies, which are candidates of near- or super-critical flows (Watarai et al. 2001; Mineshige et al. 2000; Kawaguchi 2003).

\* Example: Present Address is *katsuya.hashizume@gmail.com*

Outflow from the slim disk is of interest to recent observational and theoretical studies. It has been reported by recent observations that powerful outflows are ejected from the central engine of ULXs. Some of the bubbles/nebulae around ULXs are shock-excited via the outflow, of which the kinetic power is estimated as  $\sim 10^{39-40} \text{ erg s}^{-1}$  (Pakull & Mirioni 2002; Pakull & Mirioni 2003; Grisé et al. 2006; Abolmasov et al. 2007; Cseh et al. 2012). Since the slim disk is basically one-dimensional model, the launching outflow is not taken into consideration. Two-dimensional version of the slim disk is studied by radiation hydrodynamics (RHD) simulations (Eggum et al. 1988; Okuda 2002; Ohsuga 2006; Kawashima et al. 2009) and radiation magnetohydrodynamics simulations (Ohsuga et al. 2009; Takeuchi, Ohsuga, Mineshige 2010; Ohsuga & Mineshige 2011; Sądowski et al. 2014). Ohsuga et al. (2005; hereafter O05) for the first time demonstrated the quasi-steady super-critical accretion is feasible. The luminosity and the mass accretion rate exceed the Eddington luminosity and the critical rate.

O05 also revealed that the outflow is launched from the disk surface via the radiation force for Thomson scattering. High-velocity outflow, which is defined as the matter being blown away with speed of  $> v_{\text{esc}}$ , appear around the rotation axis, where  $v_{\text{esc}}$  is the escape velocity. However, at wide off-axis angle, huge amount of mass passes out through the outer boundary at  $500r_{\text{S}}$ , with  $r_{\text{S}}$  being Schwarzschild radius, with velocity of  $< v_{\text{esc}}$  (low-velocity outflow). Behavior of such low-velocity outflow is significant issue. If the outflowing matter continues to be accelerated and exceeds the escape velocity at a great distance, the angular size of the high-velocity outflow would increase significantly. Otherwise the gas comes back to the vicinity of the black hole and mass accretion rate would go up. In the former case, powerful outflows might excite the interstellar medium via shock, reproducing the shock-excited bubbles observed around ULXs. The mass accretion might be interrupted by the ram pressure and/or shock heating, preventing quasi-steady super-critical accretion. However, global structure and dynamics of the outflows at the large distance have not been investigated previously. This is a motivation for the present study.

Here, we perform two-dimensional RHD simulations of super-critical accretion flows and outflows. We employ large computational box of  $5000r_{\text{S}}$ . We explain basic equations and the numerical methods in §2, and display the structure of the wide-angle powerful outflows §3. Finally, §4 and §5 are devoted to discussion and conclusions.

## 2. Basic equations and numerical method

In this section, we describe basic equations of RHD and our numerical method. We employ spherical polar coordinates  $(r, \theta, \varphi)$ , where  $r$  is the radial distance,  $\theta$  is the polar angle, and  $\varphi$  is the azimuthal angle. Our numerical method is same as O05 except for the size of the computational domain. While they set the size of the domain to be  $500r_{\text{S}}$ , we extended it to  $5000r_{\text{S}}$  in order to inves-

tigate the motion of the outflows at the outer regions of  $r > 500r_{\text{S}}$ .

Since we assume axial symmetry as well as reflection symmetry with respect to the equatorial plane, the computational domain consists of spherical shells of  $r_{\text{in}} \lesssim r \lesssim r_{\text{out}}$  and  $0 \lesssim \theta \lesssim \frac{\pi}{2}$ , where  $r_{\text{in}}$  and  $r_{\text{out}}$  are set to be  $3r_{\text{S}}$  and  $5000r_{\text{S}}$ . This domain is divided into  $N_r \times N_\theta = 140 \times 96$  grid cells, though O05 employs  $N_r \times N_\theta = 96 \times 96$  grid points. The  $N_r$  grids along the radial direction are equally spaced logarithmically, while the  $N_\theta$  grids are equally distributed as satisfying  $\Delta \cos \theta = 1/N_\theta$ . Here, because the number of grid points in radial direction within  $r = 500r_{\text{S}}$  is 96, the resolution of the present work is the same as that of O05 near the black hole.

By an explicit-implicit finite difference scheme on the Eulerian grids, we numerically solve the RHD equations including viscosity terms, the equation of continuity,

$$\frac{\partial \rho}{\partial t} + \nabla \cdot (\rho \mathbf{v}) = 0, \quad (1)$$

the equation of motion,

$$\begin{aligned} \frac{\partial(\rho v_r)}{\partial t} + \nabla \cdot (\rho v_r \mathbf{v}) \\ = -\frac{\partial p}{\partial r} + \rho \left[ \frac{v_\theta^2}{r} + \frac{v_\varphi^2}{r} - \frac{GM}{(r-r_{\text{S}})^2} \right] + \frac{\chi}{c} F_0^r, \end{aligned} \quad (2)$$

$$\frac{\partial(\rho r v_\theta)}{\partial t} + \nabla \cdot (\rho r v_\theta \mathbf{v}) = -\frac{\partial p}{\partial \theta} + \rho v_\varphi^2 \cot \theta + \frac{\chi}{c} r F_0^\theta, \quad (3)$$

$$\begin{aligned} \frac{\partial(\rho r \sin \theta v_\varphi)}{\partial t} + \nabla \cdot (\rho r \sin \theta v_\varphi \mathbf{v}) \\ = \frac{1}{r^2} \frac{\partial}{\partial r} \left[ \eta r^4 \sin \theta \frac{\partial}{\partial r} \left( \frac{v_\varphi}{r} \right) \right], \end{aligned} \quad (4)$$

the energy equation of the gas,

$$\begin{aligned} \frac{\partial e}{\partial t} + \nabla \cdot (e \mathbf{v}) \\ = -p \nabla \cdot \mathbf{v} - 4\pi \kappa B + c \kappa E_0 + \eta \left[ r \frac{\partial}{\partial r} \left( \frac{v_\varphi}{r} \right) \right]^2, \end{aligned} \quad (5)$$

the energy equation of the radiation,

$$\begin{aligned} \frac{\partial E_0}{\partial t} + \nabla \cdot (E_0 \mathbf{v}) \\ = -\nabla \cdot \mathbf{F}_0 - \nabla \mathbf{v} : \mathbf{P}_0 + 4\pi \kappa B - c \kappa E_0. \end{aligned} \quad (6)$$

Here  $\rho$  is the gas mass density,  $\mathbf{v} = (v_r, v_\theta, v_\varphi)$  is the velocity,  $p$  is the gas pressure,  $M$  is the black hole mass,  $e$  is the internal energy density of the gas,  $B$  is the blackbody intensity,  $E_0$  is the radiation energy density,  $\mathbf{F}_0 = (F_0^r, F_0^\theta)$  is the radiation flux,  $\mathbf{P}_0$  is the radiation pressure tensor,  $\eta$  is the dynamical viscosity coefficient,  $\kappa$  is the absorption opacity, and  $\chi (= \kappa + \rho \sigma_{\text{T}}/m_p)$  is the total opacity, where  $\sigma_{\text{T}}$  is the Thomson scattering cross section and  $m_p$  is the proton mass. Throughout the present study, we employ  $M = 10M_\odot$ . For the absorption opacity,  $\kappa$ , we consider the free-free absorption and the bound-free absorption for solar metallicity (Hayashi et al. 1962; Rybicki & Lightman 1979; see also O05).

In addition, we use an equation of state,

$$p = (\gamma - 1)e, \quad (7)$$

where  $\gamma (= 5/3)$  is the specific heat ratio. The temperature of the gas,  $T$ , can be calculated from

$$p = \frac{\rho k_B T}{\mu m_p}, \quad (8)$$

where  $k_B$  is the Boltzmann constant and  $\mu (= 0.5)$  is the mean molecular weight.

We apply the flux-limited diffusion (FLD) approximation (Levermore & Pomraning 1981). Then, the radiation flux,  $\mathbf{F}_0$ , and the radiation pressure tensor,  $\mathbf{P}_0$ , are expressed in terms of the radiation energy density (see O05). We consider only  $r\varphi$ -component in the viscous stress tensor. The dynamical viscosity coefficient is given by  $\eta = \alpha(p + \lambda E_0)/\Omega_K$ , where  $\alpha (\equiv 0.1)$  is the viscosity parameter,  $\Omega_K$  is the Keplerian angular speed, and  $\lambda$  is the flux limiter, which becomes  $1/3$  in the optically thick limit and null in the optically thin limit. Here we note that the momentum conservation is not strictly accurate in the present simulations. This is because that, in the FLD approximation, the radiation flux is simply given as a function of the gradient of the radiation energy without being solved by conservative form. Such problem should be resolved by numerical simulations with M-1 closure method (González et al. 2007; Takahashi & Ohsuga 2013). Recently, the simulations of the radiation dominated accretion disks around black holes with M-1 closure have been performed by Sądowski et al. (2013, 2014) and McKinney et al. (2014).

The hydrodynamical terms for ideal fluid in Eqs. (1)-(5) are explicitly solved with using the computational hydrodynamical code, the Virginia Hydrodynamics One. The advective transport of radiation energy in Eq. (6) is also treated with the explicit method. In Eqs. (4)-(6), we solve the gas-radiation interaction terms, the radiation flux term and the viscous terms based on the implicit method. In order to update the radiation energy and the azimuthal component of the velocity by solving the radiative flux term and the viscosity term, we employ the Gauss-Jordan elimination for a matrix inversion.

Our initial and boundary conditions are essentially same as those of O05. We start the calculations with a hot and rarefied atmosphere, and matter is continuously injected into the computational domain through the outer disk boundary,  $r = r_{\text{out}}$  and  $0.45\pi \lesssim \theta \lesssim 0.5\pi$  (as we have mentioned above, the outer boundary is located at  $r = 500r_S$  in O05 and we employ  $r_{\text{out}} = 5000r_S$ ). Such injected matter is supposed to have a specific angular momentum corresponding to the Keplerian angular momentum at  $r = r_{\text{rot}}$ .

In the present study, we mainly investigate the case that the injected mass accretion rate at the outer boundary (mass input rate,  $\dot{M}_{\text{input}}$ ) is  $1000L_{\text{Edd}}/c^2$  and  $r_{\text{rot}}$  is  $100r_S$  (base line model). In §4.2, we discuss the results for  $\dot{M}_{\text{input}} = 1000L_{\text{Edd}}/c^2$  and  $r_{\text{rot}} = 500r_S$  (comparison model 1) as well as  $\dot{M}_{\text{input}} = 10000L_{\text{Edd}}/c^2$  and  $r_{\text{rot}} = 100r_S$  (comparison model 2).

### 3. Result

#### 3.1. Global inflow-outflow structure

Although there is no accretion disk initially, the injected matter accumulates within the computational domain. Then, the accretion disk as well as the launching outflow appears. The quasi-steady structure for base line model is shown in Fig.1, in which the color contour indicates the gas density and arrows mean velocity vectors in  $r - z$  plane. They are time-averaged in the elapsed time between  $t = 70$  sec and 200 sec (the Keplerian time at  $r = r_{\text{rot}}$  is about 0.9 sec in the present simulations because of  $M_{\text{BH}} = 10M_\odot$ ). The high density region at  $r \lesssim 500r_S$  (red and white) corresponds to super-critical accretion disk (disk region), which is radiation pressure-dominated, and geometrically and optically thick. The injected matter freely falls in the yellow region near the equatorial plane at  $r \gtrsim 500r_S$  (free-fall region), since the centrifugal force is less than the gravity. Except for the disk region and the free-fall region, we find that the matter moves outwards for the wide angle (wide-angle outflow region).

The white solid line in this figure indicates the boundary at which the radial velocity,  $v_r$ , equals to the escape velocity,  $v_{\text{esc}}$ . Above the line, the matter is blown away with speed of  $v_r > v_{\text{esc}}$  (high-velocity outflow). Although we also find outflow motion below the line, the matter cannot be released from the gravity (low-velocity outflow). Fig.1 also shows that the angular size of the high-velocity outflow broadens with an increase of the radius. The high-velocity outflow appears only at the angle of  $\theta \lesssim 35^\circ$  near the black hole ( $r \lesssim 500r_S$ ). In  $\theta \gtrsim 35^\circ$ , the matter is gradually accelerated and its velocity is over  $v_{\text{esc}}$  at the outer region. For example, the radial velocity exceeds escape velocity at  $r \gtrsim 1000r_S$  for  $\theta \sim 45^\circ$ , and we find that  $v_r$  achieves  $v_{\text{esc}}$  at  $r \sim 3000r_S$  for  $\sim 70^\circ$ . As a result, the matter is ejected from the outer boundary with  $v_r > v_{\text{esc}}$  for almost all direction ( $0^\circ \lesssim \theta \lesssim 85^\circ$ ) except for the vicinity of the equatorial plane.

Such a wide-angle high-velocity outflow at the regions of  $r \gg 500r_S$  is for the first time revealed by our present study. O05, in which the computational domain is  $500r_S$  (dotted line in Fig.1), showed the high-velocity outflow ( $v_r > v_{\text{esc}}$ ) only near the rotation axis ( $\theta \lesssim 35^\circ$ ). The radial velocity of  $\theta \gtrsim 35^\circ$  is less than the escape velocity. O05 could not reveal the behavior of such low-velocity outflow at the outer regions because of limited computational domain (see §4.1 for detail comparison).

Our present simulation succeeded in reproducing the quasi-steady super-critical disk accretion flow. Fig.2 shows the time evolution of the mass accretion rate onto the black hole (black line),

$$\dot{M}_{\text{BH}} = 2\pi r_{\text{in}}^2 \int \rho(-v_r) \sin\theta d\theta, \quad (9)$$

and the photon luminosity (green line),

$$L_{\text{ph}} = 2\pi r_{\text{out}}^2 \int F_0^r \sin\theta d\theta. \quad (10)$$

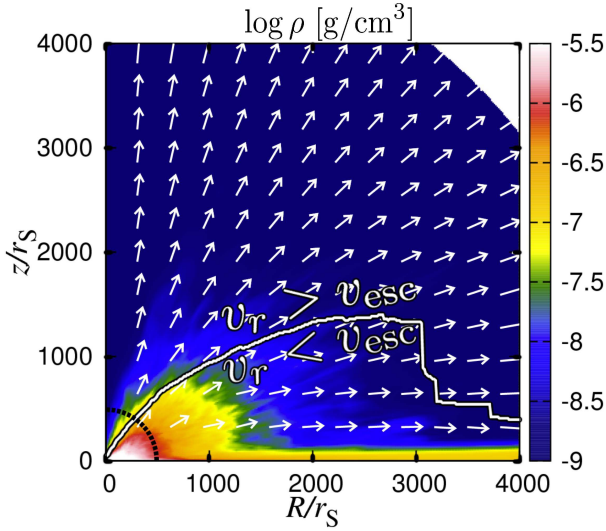


**Fig. 1.** The density distribution (color) overlaid with the velocity vectors in quasi-steady state. They are time-averaged in the elapsed time between  $t = 70$  sec and 200 sec. The white solid line indicates the boundary at which the radial velocity equals to escape velocity. Thus, the radial velocity is larger (smaller) than the escape velocity above (below) the line. The dotted line indicates the computational domain of Ohsuga et al. (2005).

The mass accretion rate is around 150 times larger than the critical accretion rate ( $L_{\text{Edd}}/c^2$ ), and the luminosity is  $\sim 2.5L_{\text{Edd}}$  in the quasi-steady state ( $t \gtrsim 60$  sec). Such results are roughly consistent with those of O05. We conclude that the wide-angle outflow does not prevent the mass accretion onto the black hole, and quasi-steady super-critical accretion is feasible.

Fig.1 also indicates that huge amount of matter is blown away by the wide-angle high-velocity outflows and energy is released not only via the radiation but also via the outflows. The blue line shows the mass escape rate,

$$\dot{M}_{\text{esc}} = 2\pi r_{\text{out}}^2 \int \rho \left\{ \begin{array}{ll} v_r & \text{for } v_r \geq v_{\text{esc}} \\ 0 & \text{for } v_r < v_{\text{esc}} \end{array} \right\} \sin\theta d\theta, \quad (11)$$

that means the ejected mass per unit time through the outer boundary via the high-velocity outflow. The kinetic power of the high-velocity outflow,

$$L_{\text{kin}} = 2\pi r_{\text{out}}^2 \times \int \left( \frac{1}{2} \rho v^2 \right) \left\{ \begin{array}{ll} v_r & \text{for } v_r \geq v_{\text{esc}} \\ 0 & \text{for } v_r < v_{\text{esc}} \end{array} \right\} \sin\theta d\theta, \quad (12)$$

are also plotted in Fig.2 (red). It is found that both the mass escape rate and the kinetic power is quasi-steady. We find  $\dot{M}_{\text{esc}} \sim 700L_{\text{Edd}}/c^2$ , which corresponding to 70% of the mass input rate and largely exceeds the mass accretion rate onto the black hole,  $\dot{M}_{\text{BH}} \sim 150L_{\text{Edd}}/c^2$ . We confirmed that gas is ejected from the super-critical accretion flows with the rate of  $\dot{M}_{\text{esc}} > \dot{M}_{\text{BH}}$ . We also find that the kinetic power of the high-velocity outflow is over the Eddington luminosity and comparable to the photon luminosity,  $L_{\text{kin}} \sim L_{\text{ph}}$ .

O05 indicated  $\dot{M}_{\text{esc}} \sim 100L_{\text{Edd}}/c^2$ . However this value

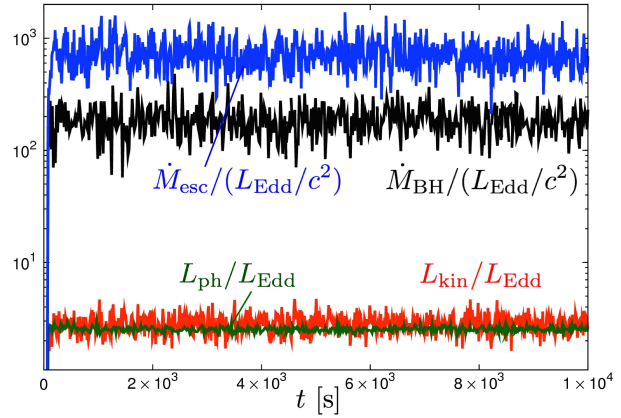


**Fig. 2.** The time evolution of the normalized photon luminosity ( $L_{\text{ph}}/L_{\text{Edd}}$ ; green), kinetic power ( $L_{\text{kin}}/L_{\text{Edd}}$ ; red), the mass accretion rate onto the black hole ( $\dot{M}_{\text{BH}}/(L_{\text{Edd}}/c^2)$ ; black) and the mass escape rate ( $\dot{M}_{\text{esc}}/(L_{\text{Edd}}/c^2)$ ; blue).

was evaluated at their outer boundary,  $r_{\text{out}} = 500r_s$ . Since the matter is accelerated at the regions of  $r > 500r_s$ , the mass escape rate is much larger in the present simulation than that in O05.

### 3.2. Radiation force

Here we show that the wide-angle outflow is driven via the radiation force. It is clearly understood by Fig.3. The upper panel of this figure indicates the ratio of the radial component of the radiation force ( $f_{\text{rad}}^r = \chi F_0^r/c$ ) and the gravity ( $|f_{\text{grav}}^r| = GM/[r - r_s]^2$ ). In the lower panel, we plot the radial component of the centrifugal force ( $f_{\text{cent}}^r = v_\phi^2/r$ ) divided by the gravity. Here, they are also time-averaged over 130 sec (70 – 200 sec). We find in the upper panel that the radiation force is dominant over the gravity in the wide-angle outflow region (see white and red). On the other hand, the centrifugal force is less effective at this region (blue in the lower panel). Since the gas pressure force is also much smaller than the radiation force, we conclude that the wide-angle outflow is mainly driven by the radiation force.

Around the rotation axis, since the radiation force exceeds the gravity near the black hole, the high-velocity outflow emerges from the inner region. In contrast, in the direction of  $\theta \gtrsim 45^\circ$ , the radiation force exceeds the gravity only at the outer region,  $r \gtrsim 1000r_s$ . Thus, the angle of  $v_r > v_{\text{esc}}$  gradually broadens with an increase of the radius, producing the wide-angle high-velocity outflow at  $r \gtrsim 4000r_s$  (see Fig.1).

Here, we note that the radiation force is less effective against freely falling matter near the equatorial plane, since the radiation does not penetrate the very optically thick material. Therefore, the radiation pressure does not prevent the free-falling motion along the equatorial plane. Indeed, we can see that the radiation force is very small at  $\theta \gtrsim 85^\circ$  and  $r \gtrsim 1000r_s$  in the upper panel of Fig.3 (blue). In the disk region ( $r \lesssim 500r_s$ ), both of the centrifugal force and the radiation force is less than the gravity (shown in yellow and green in the upper and lower panels, respec-



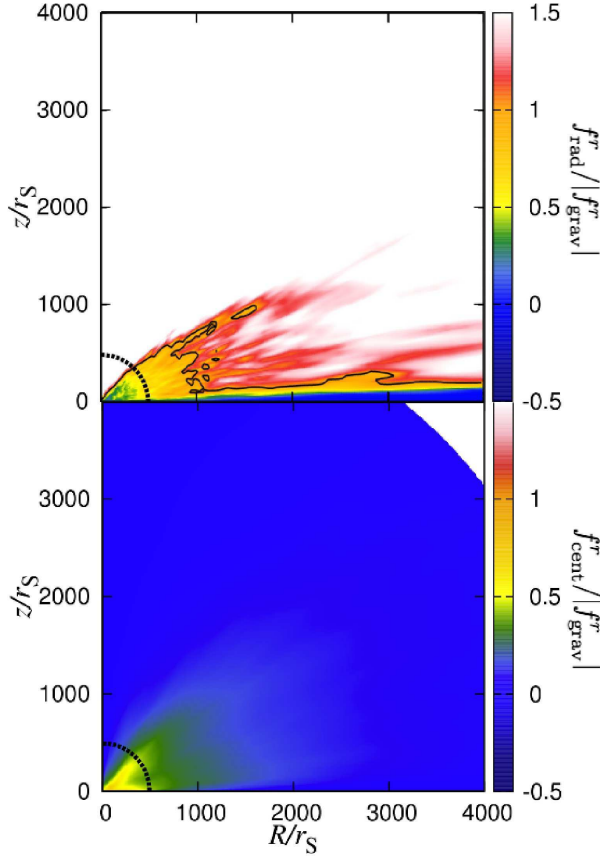


**Fig. 3.** Upper panel: the ratio of the radial component of the radiation force and the gravity. The solid line indicates a contour of unity (The outward radiation force equals the gravity). Lower panel: the radial component of the centrifugal force divided by the gravity. Both are time-averaged in the elapsed time between  $t = 70$  sec and 200 sec.

tively). However, sum of them are roughly balances with the gravity. Thus, the matter slowly accretes onto the black hole, since the angular momentum is transported via the viscosity. Such a feature has been shown by Ohsuga & Mineshige (2007).

### 3.3. Structure of wide-angle outflow

Next, we quantitatively discuss the outflow motion, as well as accretion motion. We plot in Fig.4 the  $r$ -dependent mass escape rate (blue),

$$\dot{M}_{\text{esc},r} = \int 2\pi r^2 \rho \begin{cases} v_r & \text{for } v_r \geq v_{\text{esc}} \\ 0 & \text{for } v_r < v_{\text{esc}} \end{cases} \sin\theta d\theta, \quad (13)$$

mass outflow rate (magenta),

$$\dot{M}_{\text{out},r} = \int 2\pi r^2 \rho \max[v_r, 0] \sin\theta d\theta, \quad (14)$$

and mass inflow rate (black),

$$\dot{M}_{\text{in},r} = \int 2\pi r^2 \rho \min[v_r, 0] \sin\theta d\theta. \quad (15)$$

Note that the mass accretion rate onto the black hole,  $\dot{M}_{\text{BH}}$ , and the mass escape rate,  $\dot{M}_{\text{esc}}$ , correspond to  $\dot{M}_{\text{in},r}$

and  $\dot{M}_{\text{esc},r}$  at  $r = r_{\text{in}}$  and  $r = r_{\text{out}}$ , respectively (see Eqs. [9] and [11]). The dotted line indicates the sum of the  $r$ -dependent mass inflow rate and mass outflow rate,  $\dot{M}_{\text{in},r} + \dot{M}_{\text{out},r}$ . All values are time-averaged over 130 sec ( $t = 70 - 200$  sec).

As shown in Fig.4, the mass escape rate monotonically increases with an increase of the radius. This is because that the radiation force continues to accelerate the matter, increasing the mass of the outflow with  $v_r > v_{\text{esc}}$ . Although the mass escape rate is smaller than the mass outflow rate,  $\dot{M}_{\text{esc},r} < \dot{M}_{\text{out},r}$ , within  $r \sim 3500r_S$ , we find  $\dot{M}_{\text{esc},r} \sim \dot{M}_{\text{out},r}$  at  $r \gtrsim 3500r_S$ . This implies that the velocity of almost all outflowing matter exceeds the escape velocity, and all the matter ejected from the computational domain is blown away far in the distance. Here we note that the mass escape rate as well as outflow rate at the outer boundary goes up  $\sim 700L_{\text{Edd}}/c^2$  when  $t \gtrsim 500$  sec in spite of  $\dot{M}_{\text{out},r} \sim \dot{M}_{\text{esc},r} \sim 500L_{\text{Edd}}/c^2$  in Fig.4.

In the regions of  $r \lesssim 700r_S$ , we find  $\dot{M}_{\text{out},r} > 10^3 L_{\text{Edd}}/c^2$  and  $\dot{M}_{\text{in},r} < -10^3 L_{\text{Edd}}/c^2$ . This is caused by the convective motion or circulation of the high-density gas in the disk region. The sum of the mass inflow rate and outflow rate is somewhat negative, implying that the disk matter gradually accretes towards the black hole. The flat profile of  $\dot{M}_{\text{in},r} (\sim -10^3 L_{\text{Edd}}/c^2)$  at  $r \gtrsim 1500r_S$  indicates that the injected matter freely falls along the equatorial plane.

Here, we note that sum of  $-\dot{M}_{\text{in},r}(r = r_{\text{in}})$  and  $\dot{M}_{\text{out},r}(r = r_{\text{out}})$  is about 70% of  $-\dot{M}_{\text{in},r}(r = r_{\text{out}})$ . It means that the 70% of the injected matter goes out from the computational domain and total mass in the domain continuously increases with time. The matter seems to gradually accumulate at around  $r \sim 500 - 1500r_S$ , since the gradient of the dotted line,  $\dot{M}_{\text{in},r} + \dot{M}_{\text{out},r}$ , is negative. In contrast, the flat profile of the dotted line near the black hole and outer region ( $r \gtrsim 1500r_S$ ) implies that the inflow/outflow equilibrium is achieved. Although we find that  $\dot{M}_{\text{out},r}(r = r_{\text{out}}) - \dot{M}_{\text{in},r}(r = r_{\text{in}})$  becomes  $\sim 90\%$  of mass input rate at  $t \gtrsim 500$  sec (see Fig.2), we need long-term calculations in order to examine a conclusive steady structure,  $\dot{M}_{\text{out},r}(r = r_{\text{out}}) - \dot{M}_{\text{in},r}(r = r_{\text{in}}) = \dot{M}_{\text{in},r}(r = r_{\text{out}})$ .

The upper panel of Fig.5 shows the  $r$ -dependent mass escape rate split into an angular range of  $15^\circ$ ,

$$\begin{aligned} \dot{M}_{\text{esc},r15} = 2\pi \int_{\theta-7.5^\circ}^{\theta+7.5^\circ} r^2 \rho \\ \times \begin{cases} v_r & \text{for } v_r \geq v_{\text{esc}} \\ 0 & \text{for } v_r < v_{\text{esc}} \end{cases} \sin\theta d\theta, \end{aligned} \quad (16)$$

for  $r = 100r_S$  (gray),  $500r_S$  (light green),  $2000r_S$  (light magenta), and  $4000r_S$  (blue). Here, this rate is time-averaged in the elapsed time between  $t = 70$  sec and 200 sec.

We find in this panel that the velocity of outflow is larger than the escape velocity near the rotation axis in the vicinity of the black hole. The angular size of high-velocity outflow tends to broaden with an increase of the radius. In particular, although the high-velocity outflow appears only in the direction of  $\theta \lesssim 35^\circ$  at  $r = 100r_S$ , the angular

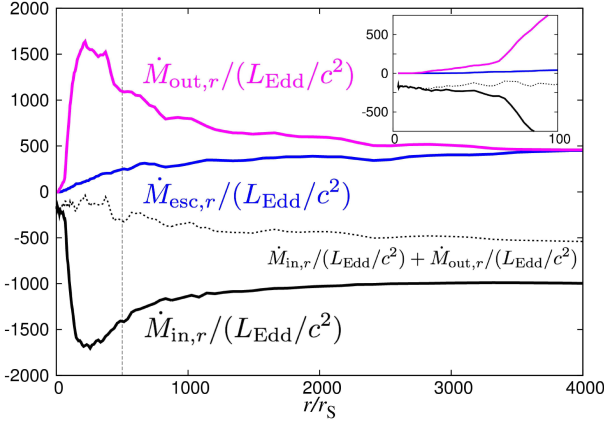


**Fig. 4.** The  $r$ -dependent the mass escape rate (blue), the mass outflow rate (magenta), the mass inflow rate (black), and the sum of mass inflow rate and mass outflow rate (dotted). All values are time-averaged over 130 sec (70 – 200 sec). The profiles of them nearer the black hole are shown in the small panel.

size of the high-velocity outflow extends up to  $\sim 20^\circ$  and  $\sim 50^\circ$  at  $r = 500r_s$  and  $2000r_s$ . Eventually, the matter is blown away with speed of  $> v_{\text{esc}}$  in the wide angle,  $0 - 85^\circ$  (see  $r = 4000r_s$ ). We find that  $\dot{M}_{\text{esc},r15}$  at  $r = 4000r_s$  is not so sensitive to the angle. It is slightly small near the rotation axis and equatorial plane and slightly enhanced around  $20^\circ$ . Note that mass flux via the high-velocity is mildly collimated (compare with sine curve [solid line]). We conclude that the mass is blown away with speed of  $> v_{\text{esc}}$  towards all direction somewhat focusing around  $20^\circ$ .

In the lower panel of Fig.5, we plot kinetic power and photon luminosity split into an angular range of  $15^\circ$ ,

$$L_{\text{kin},15} = 2\pi r_{\text{out}}^2 \int_{\theta-7.5^\circ}^{\theta+7.5^\circ} \left( \frac{1}{2} \rho v^2 \right) \times \begin{cases} v_r & \text{for } v_r \geq v_{\text{esc}} \\ 0 & \text{for } v_r < v_{\text{esc}} \end{cases} \sin \theta d\theta, \quad (17)$$

and

$$L_{\text{ph},15} = 2\pi r_{\text{out}}^2 \int_{\theta-7.5^\circ}^{\theta+7.5^\circ} F_0^r \sin \theta d\theta, \quad (18)$$

time-averaged in the elapsed time between  $t = 70$  sec and  $200$  sec. In addition to the mass, it is found that the kinetic energy is released in all direction except for the vicinity of the equatorial plane,  $\theta \gtrsim 85^\circ$ . However, in contrast that  $\dot{M}_{\text{esc},r15}$  for  $r = 4000r_s$  is small at  $\theta \lesssim 15^\circ$ ,  $L_{\text{kin},15}$  is enhanced around the rotation axis. We find that  $L_{\text{kin},15}$  is 100 times larger for  $\theta \sim 10^\circ$  than for  $\theta \sim 80^\circ$ . We also find that  $L_{\text{ph},15}$  is not so sensitive to the angle (Note that the radial component of the radiative flux,  $F_0^r$ , is mildly collimated [compare with sine curve]). As we have already mentioned, the resulting total kinetic power is comparable to the photon luminosity,  $L_{\text{kin}} \sim L_{\text{ph}}$ . Since we set the black hole mass to be  $10M_\odot$ , we have  $L_{\text{kin}} \sim 3 \times 10^{39}$  [erg/s].

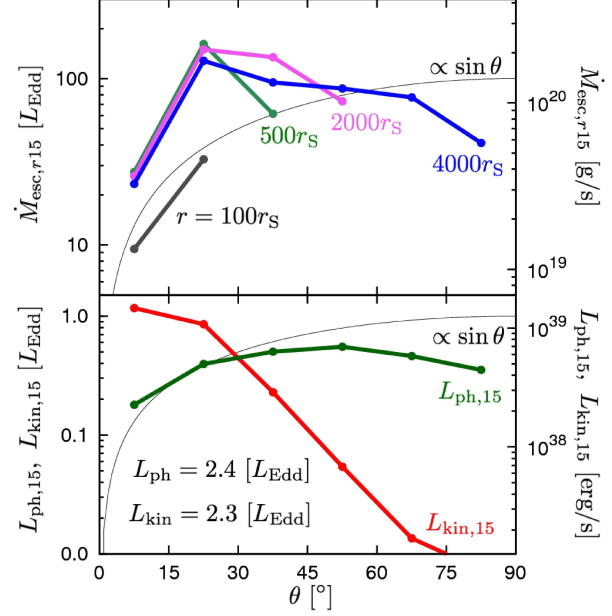


**Fig. 5.** Upper panel: mass transported outwards per unit time via the high-velocity outflow as a function of angle for  $100r_s$  (gray),  $500r_s$  (light green),  $2000r_s$  (light magenta), and  $4000r_s$  (blue). Lower panel: kinetic energy transported outwards via the high-velocity outflow per unit time as a function of the angle (red). The radiation flux integrated with respect to each  $15^\circ$  is also plotted (green). All values are time-averaged over 130sec (70 – 200 sec).

## 4. Discussion

### 4.1. Comparing with Ohsuga et al. (2005)

Here, we compare our results with O05. In O05, although the huge amount of the gas is ejected from the their computational domain,  $r = 500r_s$ , the velocity of the outflowing matter does not exceed the escape velocity except for the high-velocity outflow near the rotation axis. At the outer boundary, mass outflow rate is about several  $100L_{\text{Edd}}/c^2$  but  $\dot{M}_{\text{esc}} \sim 100L_{\text{Edd}}/c^2$ . Hence, it is not clear that whether such a low-velocity outflow come back to the neighborhood of the black hole or is blown away due to the radiation force. In the present study, the occurrence of the wide-angle high-velocity outflow is for the first time revealed. The low-velocity outflow is accelerated at the outer region and its velocity exceeds the escape velocity at  $r \gtrsim 4000r_s$ .

Our resulting flow structure is distinct from that of O05 at around  $r = 300 - 500r_s$ . Upper and lower panels in Fig.6 display the time-averaged (40 sec) density distribution overlaid with the velocity vectors of the present work and O05. There is no remarkable difference in the vicinity of the black hole ( $r \lesssim 100r_s$ ). However, high-density region (white and yellow) is wider in the present study than in O05, (see the region of  $r \sim 300 - 500r_s$ ). This is caused by that the outer boundary is located at  $r = 500r_s$  in O05. In our simulations, although the time-averaged velocity is outward as shown in the top panel, circular motion occurs around  $r \sim 300 - 700r_s$ . In contrast, since the matter that

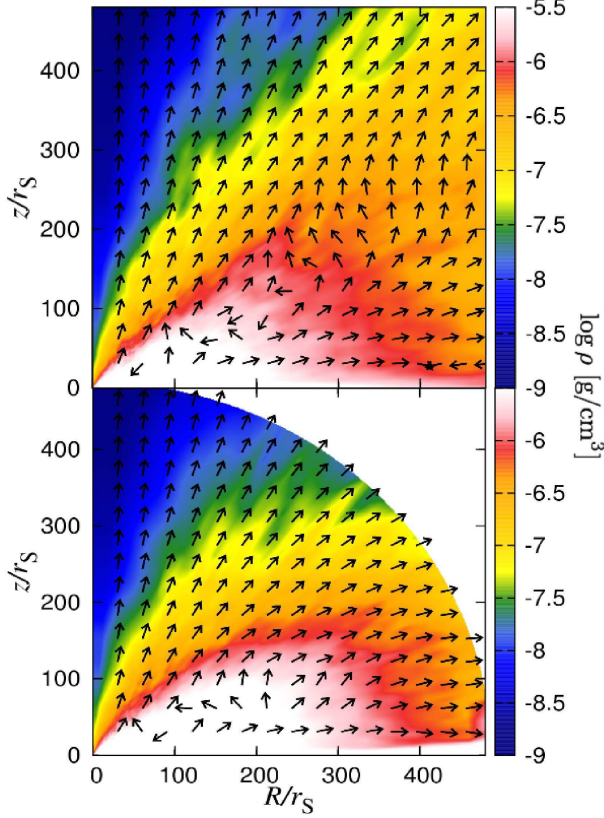


**Fig. 6.** Time averaged density distribution overlaid with the time-averaged velocity vectors of the present simulation (upper panel) and O05 (lower panel).

goes out through the boundary can not come back, the small domain in O05 tends to decrease the density.

#### 4.2. Wide-angle outflows of comparison models

Next, we show the results of comparison models 1 and 2. In comparison model 1, we employ  $r_{\text{rot}} = 500r_s$ . Then, the centrifugal force tends to prevent the free-falling motion around  $500r_s$ . Although the disk region expands in the horizontal direction, the super-critical flow is realized. Resulting photon luminosity is  $\sim 2L_{\text{Edd}}$  and the mass accretion rate onto the black hole is  $\sim 100L_{\text{Edd}}/c^2$ . We plot  $\dot{M}_{\text{esc},r15}$ ,  $L_{\text{kin},15}$ , and  $L_{\text{ph},15}$  in Fig.7. In the upper panel of this figure, we find that the angular size of the high-velocity outflow increases with an increase of the radius, and wide-angle high-velocity outflow ( $\theta \lesssim 85^\circ$ ) appears at  $r \gtrsim 4000r_s$ . We also find that  $L_{\text{kin},15}$  is mildly collimated in contrast with  $L_{\text{ph},15}$ . Such tendency is basically similar with the base line model. The kinetic power and the photon luminosity of this model are  $1.8L_{\text{Edd}}$  and  $2.1L_{\text{Edd}}$ , respectively. These values are also similar to those in the base line model.

In the comparison model 2, we set the mass input rate to be  $10000L_{\text{Edd}}/c^2$  and  $r_{\text{rot}}$  is kept  $100r_s$ . In this model, global structure of the outflow drastically changes. Huge amount of the matter is injected within  $r = 100r_s$  and mass accretion rate onto the black hole becomes very large,

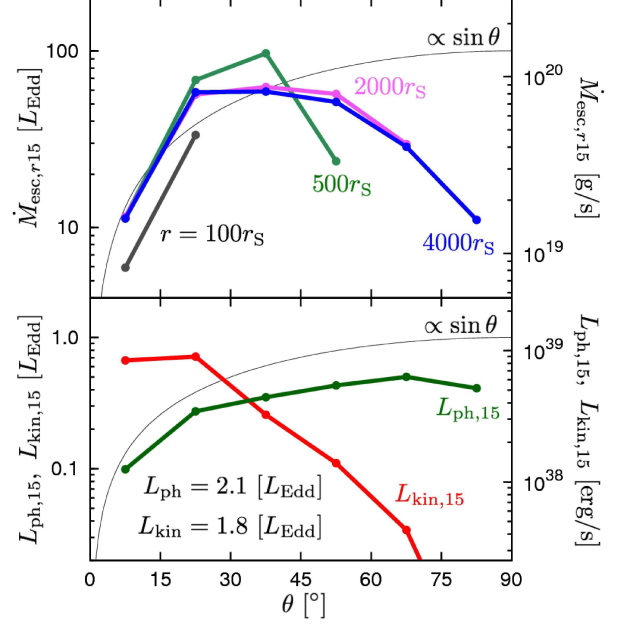


**Fig. 7.** Same as Fig.5 but for comparison model 1, in which we employ  $r_{\text{rot}} = 500r_s$ .

$\dot{M}_{\text{BH}} \sim 700L_{\text{Edd}}/c^2$ . Then, the enhanced radiation force in cooperation with the centrifugal force blows away the disk matter in the horizontal direction (horizontal outflow). In the top panel in Fig.8, we find  $\dot{M}_{\text{esc},r15}$  is enhanced in the direction of  $\theta \gtrsim 70^\circ$ . This horizontal outflow raises  $L_{\text{kin},r15}$  for  $\theta \gtrsim 70^\circ$  (see bottom panel in Fig.8), leading to the large kinetic power of  $L_{\text{kin}} \sim 13L_{\text{Edd}}$ , which is larger than the photon luminosity. However, such horizontal outflow might disappear if we employ larger  $r_{\text{rot}}$ , since, then, the disk region expands in the horizontal direction and the horizontal radiation force is reduced due to the large optical thickness of the disk matter. In order to make clear the point, we should perform the simulations with  $r_{\text{rot}} \gg 1000r_s$ . Such simulations require much longer computation times because of long viscosity timescale.

#### 4.3. Bubbles around ultra-luminous X-ray sources

By our global RHD simulations of super-critical flows around stellar mass black holes, we revealed the wide-angle, powerful outflows launched from the accretion disks via the radiation force. Such outflows would evolve into the bubbles as observed around some ULXs.

Some bubbles around ULXs are thought to be excited by the shock/outflow (Pakull & Mirioni 2002; Pakull & Mirioni 2003; Grisé et al. 2006; Abolmasov et al. 2007; Cseh et al. 2012). Recently, Cseh et al. (2012) estimated the kinetic power required for the shock-excited bubbles associated with a ULX, IC 342 X-1, to be  $\sim 3 \times 10^{39} \text{ erg s}^{-1}$  using the bubble theory (Weaver et al. 1977). This is consistent with the kinetic power seen in our model. In addition, the observed X-ray luminosity of the central source is the same order,  $\sim 5 \times 10^{39} \text{ erg s}^{-1}$ , which is also consistent with our model, where the radiation luminosity and kinetic power are comparable. Our



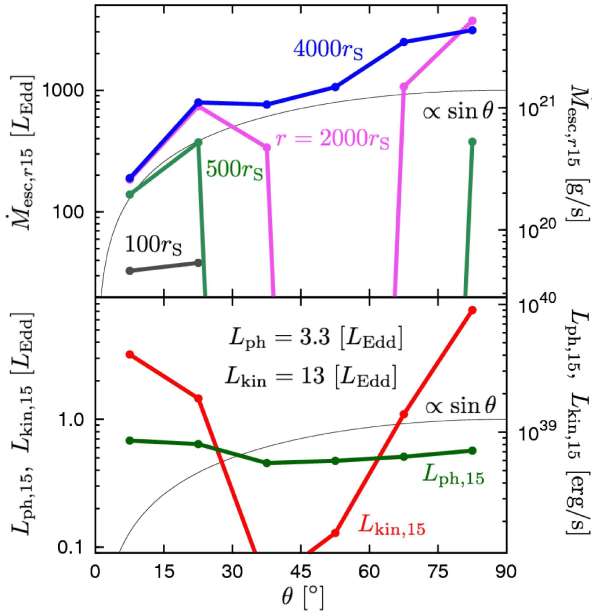


**Fig. 8.** Same as Fig.5 but for comparison model 2, in which we suppose the mass input rate to be  $1000L_{\text{Edd}}/c^2$ .

results nicely fit the observed properties of bubbles around ULXs. And therefore, our model supports a hypothesis that ULXs are powered by the super-critical accretion onto stellar mass black holes.

Another hypothesis of ULXs is the intermediate mass black holes (IMBHs) surrounded by sub-critical accretion disks. Then, large X-ray luminosity can be explained since the Eddington luminosity is about  $10^{41} \text{ erg s}^{-1}$  for  $M_{\text{BH}} = 1000 M_{\odot}$ . However, driving mechanism of the powerful outflows from the sub-critical disks are not understood yet. Also, the mechanism of energy conversion from the X-ray to the outflow is not resolved yet.

Interestingly, Cseh et al. (2014) found a jet-like structure around a ULX Holmberg II X-1. Since the nebula itself is not always excited by the shock, the direct comparison may be difficult. Nevertheless, the observed bipolar structure is reminiscent of what is seen in our model (Fig. 5), where the kinetic power is higher around the polar direction. The required kinetic power for the observed jet component ( $\sim 2 \times 10^{39} \text{ erg s}^{-1}$ ) is also similar to that obtained in our model. It is noted that such a structure is found not only around ULXs, but also around a microquasar, NGC 7793 S26, for which the super-critical accretion has been suggested (Pakull et al. 2010; Soria et al. 2010).

Some of ULXs show the time variation in X-ray band. Middleton et al. (2013) suggested that such variation is induced by the clumpy structure in the disk wind. In their model, ULXs exhibit the soft spectra and time variation for off-axis observers. In contrast, face-on observers detect the hard spectra and weak time variation (see also Sutton et al. 2013a; 2013b). Although the present work focus on the time-averaged structure, our simulations show the messy structure in the wide-angle

outflow. This is also consistent with the observations of ULXs. However, spatial resolution in the present study is not enough to resolve the clumpy structure in detail. Takeuchi, Ohsuga, Mineshige (2013) demonstrated clumpy disk wind launched from the super-critical disks by high-resolution simulations (see also Takeuchi, Ohsuga, Mineshige 2014). Thus, we stress again that our model supports the model of the super-critical accretion onto the stellar mass black holes in ULXs.

## 5. Conclusions

By performing two-dimensional RHD simulations with large computational box,  $r = 5000r_s$ , we investigate the wide-angle, powerful outflow launched from the super-critical accretion disks. The strong radiation force drives the disk wind out in all directions ( $\theta \sim 0 - 85^\circ$ ) except for the vicinity of the equatorial plane, in which the matter accretes inwards. The angular size of the high-velocity outflow, of which the outflowing velocity is larger than the escape velocity, broadens with an increase of the distance from the black hole. The outflow around the rotation axis is effectively accelerated and exceeds the escape velocity near the black hole. In contrast, at the larger polar angle, the matter continues to be gradually accelerated and attains the escape velocity at a distance of a few thousand Schwarzschild radius. Since the high-velocity outflow does not prevent the mass accretion along the equatorial plane, quasi-steady super-critical accretion onto the black hole is realized.

Due to the wide-angle high-velocity outflow, the mass and kinetic energy is ejected in all directions. However, the kinetic power is larger in the polar direction than in the horizontal direction. The kinetic power is comparable to the photon luminosity, and is a few times larger than the Eddington luminosity, which corresponds to  $\sim 10^{39} - 10^{40} \text{ erg s}^{-1}$  for the stellar mass black holes. Our results nicely fit the recent observations of shock-excited bubbles around ULXs. Thus, our model supports a hypothesis that ULXs are powered by the super-critical accretion onto stellar mass black holes.

We would like to thank the anonymous reviewer for many helpful comments. Numerical computations were carried out on XT4 and XC30 system at the Center for Computational Astrophysics (CfCA) of National Astronomical Observatory of Japan. This work is supported by Grant-in-aids from the Ministry of Education, Culture, Sports, Science, and Technology (MEXT) of Japan, No. 24740127 (KO), No. 24740117, 25103515 (MT).

## References

- Abolmasov, P., Fabrika, S., Sholukhova, O., & Afanasiev, V. 2007, *Astrophys. Bull.*, 62, 36
- Abramowicz, M. A., Czerny, B., Lasota, J. P., & Szuszkiewicz, E. 1988, *ApJ*, 332, 646



- Cseh, D., Corbel, S., Kaaret, P., et al. 2012, *ApJ*, 749, 17
- Cseh, D., Kaaret, P., Corbel, S., et al. 2014, *MNRAS*, 439, L1
- Eggum, G. E., Coroniti, F. V., & Katz, J. I. 1988, *ApJ*, 330, 142
- González, M., Audit, E., & Huynh, P. 2007, *A&A*, 464, 429
- Grisé, F., Pakull, M., & Motch, C. 2006, *The X-ray Universe 2005*, 604, 451
- Hayashi, C., Hōshi, R., & Sugimoto, D. 1962, *Progress of Theoretical Physics Supplement*, 22, 1
- Ichimaru, S. 1977, *ApJ*, 214, 840
- Kawaguchi, T. 2003, *ApJ*, 593, 69
- Kawashima, T., Ohsuga, K., Mineshige, S., et al. 2009, *PASJ*, 61, 769
- Levermore, C. D., & Pomraning, G. C. 1981, *ApJ*, 248, 321
- McKinney, J. C., Tchekhovskoy, A., Sadowski, A., & Narayan, R. 2014, *MNRAS*, 441, 3177
- Middleton, M. J., Miller-Jones, J. C. A., Markoff, S., et al. 2013, *Nature*, 493, 187
- Mineshige, S., Kawaguchi, T., Takeuchi, M., & Hayashida, K. 2000, *PASJ*, 52, 499
- Narayan, R., & Yi, I. 1994, *ApJL*, 428, L13
- Ohsuga, K. 2006, *ApJ*, 640, 923
- Ohsuga, K., & Mineshige, S. 2007, *ApJ*, 670, 1283
- Ohsuga, K., & Mineshige, S. 2011, *ApJ*, 736, 2
- Ohsuga, K., Mineshige, S., Mori, M., & Kato, Y. 2009, *PASJ*, 61, L7
- Ohsuga, K., Mori, M., Nakamoto, T., & Mineshige, S. 2005, *ApJ*, 628, 368
- Okuda, T. 2002, *PASJ*, 54, 253
- Pakull, M. W., & Mirioni, L. 2002, *astro-ph/0202488*
- Pakull, M. W., & Mirioni, L. 2003, *Revista Mexicana de Astronomía y Astrofísica Conference Series*, 15, 197
- Pakull, M. W., Soria, R., & Motch, C. 2010, *Nature*, 466, 209
- Rybicki, G. B., & Lightman, A. P. 1979, *Radiative Processes in Astrophysics* (New York: Wiley)
- Sądowski, A. 2009, *ApJS*, 183, 171
- Sądowski, A., Narayan, R., Tchekhovskoy, A., & Zhu, Y. 2013, *MNRAS*, 429, 3533
- Sądowski, A., Narayan, R., McKinney, J. C., & Tchekhovskoy, A. 2014, *MNRAS*, 439, 503
- Shakura, N. I., & Sunyaev, R. A. 1973, *A&A*, 24, 337
- Soria, R., Pakull, M. W., Broderick, J. W., Corbel, S., & Motch, C. 2010, *MNRAS*, 409, 541
- Sutton, A. D., Roberts, T. P., Gladstone, J. C., et al. 2013, *MNRAS*, 434, 1702
- Sutton, A. D., Roberts, T. P., & Middleton, M. J. 2013, *MNRAS*, 435, 1758
- Takahashi, H. R., & Ohsuga, K. 2013, *ApJ*, 772, 127
- Takeuchi, S., Ohsuga, K., & Mineshige, S. 2010, *PASJ*, 62, L43
- Takeuchi, S., Ohsuga, K., & Mineshige, S. 2013, *PASJ*, 65, 88
- Takeuchi, S., Ohsuga, K., & Mineshige, S. 2014, *PASJ*, 40
- Watarai, K.-y., Mizuno, T., & Mineshige, S. 2001, *ApJL*, 549, L77
- Weaver, R., McCray, R., Castor, J., Shapiro, P., & Moore, R. 1977, *ApJ*, 218, 377